1   **Revealing Dendritic pattern formation in Ni, Fe and Co alloys**

2   **using synchrotron tomography**

3   Authors

4   **M.A. Azeem[a,b], P.D. Lee[a,b,*], A.B. Phillion[c], S. Karagadde[a,d], P. Rockett[a], R.C. Atwood[e], L.**

5   **Courtois[a,b], K.M. Rahman[f] and D. Dye[f]**

6   [a]School of Materials, The University of Manchester, Oxford Road, Manchester, M13 9PL, UK

7   [b]Research Complex at Harwell, RAL, Didcot, OX11 0FA, UK

8   [c]Department of Materials Science and Engineering, McMaster University, Hamilton, ON, Canada

9   [d]Department of Mechanical Engineering, Indian Institute of Technology Bombay, 400076, India
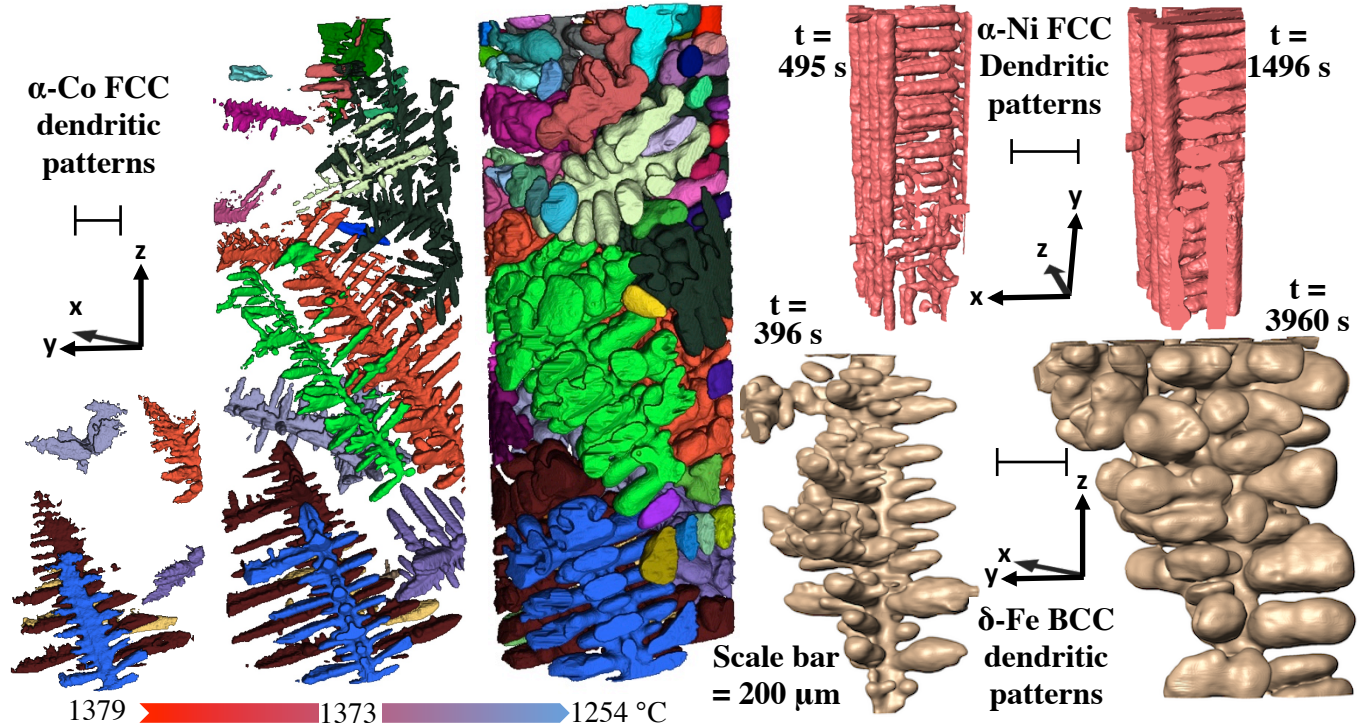
10   [e]Diamond Light Source Ltd., Harwell Science and Innovation Campus, Didcot, OX11 0DE, UK

11   [f]Department of Materials, Royal School of Mines, Imperial College London, Prince Consort Road,

12   London SW7 2BP, UK

13   ***Corresponding email: peter.lee@manchester.ac.uk**

14

15

16   **Abstract**   The microstructural patterns formed during liquid to solid phase transformations control

17   the properties of a wide range of materials. We developed a novel methodology that allows *in situ*

18   quantification of the microstructures formed during solidification of high temperature advanced

19   alloys. The patterns formed are captured in 4D (3D plus time) using a methodology which exploits

20   three separate advances: a bespoke high temperature environment cell; the development of high X-ray

21   contrast alloys; and a novel environmental encapsulation system. This methodology is demonstrated

22   on Ni, Fe, and Co advanced alloy systems, revealing dendritic pattern formation. We present detailed

23   quantification of microstructural pattern evolution in a novel high attenuation contrast Co-Hf alloy,

24   including microstructural patterning and dendrite tip velocity. The images are quantified to provide

25   4D experimental data of growth and coarsening mechanisms in Co alloys, which are used for a range

26   of applications from energy to aerospace.

27

28   **Keywords:** Superalloys; synchrotron tomography; interfacial patterns; 4D imaging; dendritic microstructures

29

α-Co FCC dendritic patterns

1379 ← → 1373 ← → 1254 °C

α-Ni FCC Dendritic patterns
t = 495 s
t = 1496 s

t = 396 s
t = 3960 s

Scale bar = 200 μm

δ-Fe BCC dendritic patterns

30   **1. Introduction**

31   The patterns that form as materials transform from a liquid to solid directly affect the final properties

32   of material, be it a snowflake or aeroengine gas turbine (AGT) blade. Dendrites are one of the most

33   prevalent microstructural morphologies formed, for example in nickel superalloy AGTs [1] to lithium

34   depositing out in a battery [2]. The *in situ* observation of the patterns formed during the

35   transformation from liquid to solid phase, or solidification, was first performed using transparent

36   organic liquids (metallic analogues) [3–5] and optical microscopes. These results enabled the

37   validation of solidification models linking constitutional undercooling due to solute build-up with

38   interface motion, and the resulting crystal morphologies [4,6]. In areas such as the study of colloids,

39   organic analogue techniques continue to provide novel insights into the kinetic and morphological

40   aspects of crystal growth, and real-time, 2D full-field data of thermal and compositional distributions

41   [7]. However, in optically opaque systems, from magma to metallic alloys, other techniques are

42   required.

43   The first direct observations of dendritic pattern growth in metallic systems were captured in 2D using

44   *in situ* radiography in an Al-30wt% Cu alloy [8]. Subsequently, there have been many radiographic

45   studies of low temperature alloys using laboratory and synchrotron X-ray sources, including

46   elucidation of the growth of secondary phases [9] and defects such as porosity [10]. However, even

47   with radiography there is a paucity of studies on high melting point alloys, with only a few on Fe [11].

48   X-ray radiography is fast, but it requires thin samples that constrain the evolving microstructures, both

49   by restricting the orientation of patterns formed and by altering the growth kinetics. During the last

50   decade, there has been a dramatic rise in the use of X-ray tomography (often termed X-ray

51   microtomography (XMT or µCT), X-ray computed tomography (XCT), or synchrotron computed

52   tomography (sCT)) to study the evolution of microstructures during solidification. Through recent

53   advances in synchrotron X-ray facilities and iterative reconstruction algorithms, it is now possible to

54   perform fast 4D (3D + time/stress/temperature) tomography on low temperature (<800 °C) metallic

55   alloys as they solidify [12,13]. Some researchers have also studied the influence of deformation on

56   semi-solid alloys [14–16]. These X-ray radiographic and tomographic investigations have helped to

57   inform and validate many new mathematical models developed for low temperature solidification

58   microstructures [17–19] and defects [10] in metals.

59   Most 4D solidification studies of metallic systems have been performed on Al-Cu based alloys [20].

60   These alloys provide excellent attenuation contrast between the solidifying face centred cubic (FCC)

61   α-phase and the liquid. Although the morphological and kinetic aspects observed via the *in situ*

62   tomography can be correlated with industrially viable Al alloys, there is no confirmation that the

63   results can be extended to other FCC systems that solidify at very high temperatures. High

64   temperature alloys such as nickel superalloys, cobalt superalloys, and iron alloys have yet to be

65   studied in the semi-solid state using 4D imaging, although high temperature solid state investigations

66   have been performed[21]. Understanding pattern formation during the solidification of these high

67   temperature advanced alloys is critical to predicting their strength, and preventing the formation of

68   solidification defects such as freckles [17,22], and grain mis-orientation during directional (DX) and

69   single crystal (SX) growth [23,24].

70   There is also an extensive field of modelling of pattern formation in high temperature advanced alloys

71   [1,25–29]. However, these computational simulations have only been validated against long-chain

72   organic analogues or low melting point metallic analogues [17]. Unfortunately, these analogue

73   systems have very different diffusion coefficients and interfacial energies as compared to high

74   temperature alloy systems. Thus, the possibility to visualize the formation of such defects/morphology

75   *in situ* in alloy systems based on Ni, Fe and Co could dramatically advance the design and production

76   of new superalloys.

77   In this study, a methodology incorporating three main advances is provided for tomographic

78   examination of the solidification patterns in high temperature alloys with melting points exceeding

79   1300 °C: (a) design criteria for high X-ray attenuation contrast alloys; (b) the development of an

80   environmental cell enabling the combination of high temperature solidification tests and synchrotron

81   X-ray tomography; and (c) a specimen environmental encapsulation system. These innovations are

82   applied to study the evolving solidification patterns in Ni, Fe and Co alloys in 4D (3D plus time).

83   **2.   Materials and Methods**

84   **2.1. Alloy Design**

85   The majority of commercial Ni, Fe, and Co alloys form solidification phases with negligible X-ray

86   attenuation variation between them and the interdendritic liquid, making X-ray tomographic

87   characterization highly challenging. To perform 4D imaging of solidification in these materials, a

88   bespoke alloy must be used that meets four criteria: (a) the primary phase must contain little or no

89   solute, (b) at the first invariant reaction temperature there must be 40% - 60% liquid, (c) the X-ray

90   attenuation characteristics of the solute must be markedly different from the solidifying grains, and (d)

91   the primary phase that appears during solidification must be face centred cubic (body centred cubic in

92   the case of Fe). Criteria (a), (b) and (c) are necessary for achieving high X-ray contrast, while (d) is

93   essential for mimicking the solidification behaviour of alloys used in AGTs and industrial gas turbines

94   (IGTs).

95   During solidification, the solubility of the primary phase is interpreted in terms of the partition

96   coefficient, k, where $k=C_s/C_L$, where C_s and C_L are the concentration of solute in the solid and liquid

97   respectively, as shown in supplementary Fig. S1a. To meet criterion (a), the value of k must be quite

98   small, which also implies that criterion (b) is respected. For criterion (c), each element's characteristic

99   X-ray absorption edges are exploited. Using a monochromatic beam just above this absorption edge
100   enables clear identification between one phase and another. Second, when a polychromatic (*white*) X-
101   ray spectrum interacts with materials, different phases absorb different amounts of X-rays. This is
102   known as non-characteristic X-ray interaction. Consequently, depending on the alloy system, either a
103   *white* beam or a monochromatic X-ray beam with an energy just above one of the characteristic edges
104   may be used for achieving a good contrast between the solid and liquid phases.

105   To develop the high X-ray contrast Ni, Fe and Co alloys, various metallic elements were examined.
106   For Co, of the elements having smaller atomic numbers, only Mg forms a eutectic with very small *k*.
107   However, Co and Mg have nearly identical non-characteristic X-ray absorption behaviour and both
108   lack absorption edges at X-ray energies found at high-energy synchrotron beamlines, such as the I12
109   at the Diamond Light Source where the experiments were conducted. Of the elements having larger
110   atomic number than Co, only Hf fits the stated criteria. For the Co-Hf system [30,31], photon energies
111   in the range of 65 to 80 keV were found to yield a substantial attenuation difference between the
112   solidifying α-Co dendrites and Hf rich interdendritic liquid. This difference arises mainly as a result of
113   the *k*-absorption edge of Hf at 65.351 keV [32]. Similar arguments can be made for Ni and Fe.

114   In the present study, Ni-14 wt.%Hf, Fe-11 wt.%Hf and Co-18 wt.%Hf alloys were chosen for 4D
115   imaging. The Co-Hf alloy used in this investigation was obtained by induction melting and
116   conventional casting in an oxide (Al_2O_3/ZrO_2) crucible followed by air-cooling. The Ni-Hf and Fe-Hf
117   alloys were prepared in a vacuum arc melter using induction melted Ni-Hf and Fe-Hf master alloys,
118   respectively. The cylindrical samples for the *in situ* solidification trials were extracted from the
119   middle section of the as-cast sample.

120   **2.2. High temperature environmental cell and experimental setup for *in situ* XCT**

121   The high temperature environmental cell developed in this study consists of two modules, a sample
122   module and a heating module, and achieves a number of design requirements. These include the
123   ability for *in situ* XCT of solidifying alloys with melting point exceeding 1300 °C, slow cooling rates
124   on the order of 10^{-2} °Cs^{-1}, thermal precision of ±0.5 °C over a sample length of at least 10 mm, and
125   easy integration with bespoke mechanical rigs such as the P2R [15,33] for in situ thermo-mechanical
126   investigations in the semi-solid or solid states.

127   The sample module (Fig. 1a), consists of an encapsulated cylindrical sample (1.4 mm ø x 8 mm) that
128   is centrally seated and supported by an alumina sleeve and further supported by an alumina sample
129   mount 60 mm in height. Encapsulation was required to minimize oxidation and to contain the
130   specimen safely in liquid state. Each cylindrical sample was encapsulated in a 1.5 mm internal
131   diameter quartz tube (Fig. 1b) filled with Ar gas. Within the encapsulation, the metallic sample was
132   supported by using a glass rod which in turn was fused to one end of the quartz tube.

133   The heating module is shown in Fig. 2a, with the sample module inserted. The environmental cell

134   setup on the I12 beamline at the Diamond Light Source is shown in Fig. 2b. In this device, porous

135   insulation fibre is enclosed in a water-cooled stainless steel shell to house a centrally placed u-shaped

136    $MoSi_2$ high current heating element. $MoSi_2$ heating elements were chosen due to their high heat

137   density and high temperature (> 1000 °C) stability in both oxidizing [34,35] and reducing

138   environments [35]. Temperature was controlled by two R-type thermocouples placed at about 3 mm

139   from the sample surface. The sample is separated from the heating element using a central dense

140   alumina ceramic column. Further, to isolate the environmental cell chamber from the ambient

141   atmosphere, fused quartz faceplates, 0.5 mm thick, were placed over square 10 mm X-ray windows.

142   During the *in situ* high temperature solidification experiment, a 0.0165 nm (75 keV) monochromatic

143   X-ray beam with PCO edge camera at a pixel size of 1.3 μm was used for tomographic imaging with

144   900 projections and 0.1 s exposure. The experiment was conducted as follows. First, the sample was

145   heated to 1400 °C, held isothermally for 10 minutes, and then cooled at a rate of 0.05 °Cs^{-1}.

146   Concurrently, a series of X-ray tomographic images were acquired. The imaging conditions described

147   above allowed for acquisition of 27 tomograms within the semi-solid regime. The reconstructions

148   were performed by standard filtered back projection [36].

149   To improve the sample alignment, and to ensure safe operation resulting from the high temperatures,

150   thermal modelling of the environmental cell was performed using SolidWorks[37] software.

151   Boundary conditions were set on the insulating fibre block (50 °C) and heating element surface (1800

152   °C). The model included radiative heat transfer, but the contact thermal resistance between the mating

153   surfaces was ignored. The modelled temperature profile in the central block of the environmental cell

154   is shown in Supplementary Fig. S2a. In addition to isolating the sample from the heating elements, the

155   central alumina core was observed to promote radiative heating, homogenizing the temperature across

156   the central sample volume. The temperature profile across the entire quartz tube is shown in

157   Supplementary Fig. S2b. Based on the model results, the location of the X-ray field of view was

158   chosen such that there was minimum thermal gradient within the imaged volume. The model

159   predicted < 3 °C variation across sample height in the FOV.

160   **3.   Results and Discussion**

161   **3.1. Methodology Demonstration**

162   The *in situ*, 4D evolution of patterns during the liquid to solid phase transformation in each of these

163   alloys is shown in Fig. 3 and animated for the case of Co-Hf alloy in Supplementary Movie 1. The

164   corresponding as-acquired 2D images from the middle of the Co specimen are shown in

165   Supplementary Movie 2. These results demonstrate the methodology of combining a bespoke high

166   temperature furnace with X-ray translucent windows, custom designed high X-ray attenuation

167   contrast alloys, encapsulation system and high-speed synchrotron X-ray tomographic imaging to
168   capture solidification pattern evolution in high temperature alloys.

169   The formation of dendritic patterns in solidifying Ni and Fe alloys shown in Fig. 3a-d captures the
170   formation of primary, secondary and tertiary dendritic arms in these alloys. The alloys were solidified
171   at a relatively slow cooling rate of 0.05 °Cs^{-1}. In Ni, this cooling rate is sufficient to induce single
172   crystal growth as can be seen in Fig 3a and b. In this experiment, solidification begins with the
173   nucleation of a grain on the sample surface, forming dendrites which branch into secondaries in the
174   horizontal plane, which in turn form tertiary arms, which grow quickly upwards in the available
175   sample space ahead forming a forest of single crystal primary dendrites. These dendrites grow
176   vertically upwards, almost perpendicular to the sample axis (*z*). The resulting structure is an
177   interlocking dendritic mesh extending across the entire sample. The growth of secondary arms is
178   limited by solute interaction with the neighbouring patterns; several instances of direct tip-tip
179   interaction can also be observed.

180   The growth of a BCC δ-Fe primary dendrite under identical solidification conditions at the beginning
181   and late stages of solidification are shown in Fig.3c and d. These images show how the evolving
182   patterns are dominated by pattern thickening, coalescence and coarsening in the late stages of
183   solidification, as quantified previously in magnesium[38] and other light alloys[13]. Further, they
184   allow the coarsening kinetics to be quantified for the first time in an Fe alloy.

185   **3.2. Morphological Aspects of Dendrite Growth of Co alloys**

186   Having demonstrated that the methodology is applicable to Ni and Fe, we will use the Co alloy as an
187   example to demonstrate how detailed mechanistic and quantitative patterning data can be extracted to
188   inform and validate models.

189   **3.2.1.   Qualitative observations of Co solidification and dendritic pattern formation**

190   Figure 3e-h shows the evolution of Co dendrites during solidification at a cooling rate of 0.05 °Cs^{-1}.
191   Four images are provided, spanning 125˚C and an evolution in fraction solid from 1.6% to 40.9%.
192   The observed four-fold symmetry is characteristic of an FCC structure. The dendrites nucleate on the
193   sample surface and grow inwards with no discernible preferred orientation relative to the sample axis.
194   A 20-30 μm Hafnium oxide layer was present on the sample surface, as characterised by post-
195   solidification SEM-EDX examination. This oxide layer was visible in the tomograms due to
196   attenuation difference even when the sample was molten; therefore, we hypothesise that this oxide
197   assists nucleation of the α-Co phase.

198   The first grain to nucleate and grow is labelled as G1 in Fig. 3e. Note that two dendrites are marked as
199   G1 (coloured blue and brown) since the 4D images reveal that they are both part of the same single
200   crystal. We hypothesise this since both have identically aligned primary directions. The secondary

201   arms also have the identical 4-fold symmetry directions, further confirming they are part of the same
202   crystal. These two primary dendrites will have started from a nucleus on the bottom surface, which
203   initially forms a single primary arm, most likely the brown one since it is larger, that then forms
204   secondaries, and subsequently, tertiary dendrite arms. One of these tertiary arms, just sufficiently far
205   from the original primary, will grow quick with the same crystal orientation as the first primary
206   (brown). This tertiary becomes another primary dendrite (G1, blue), establishing the repeating 4-fold
207   patterning of an FCC crystal structure.

208   Similarly, the orange and the light green dendrites (Fig. 3f) form part of a single grain (G2). A third
209   large grain, depicted in dark green (G3) has sufficient space to form a remarkable pattern of primary,
210   secondary and tertiary arms forming in a 4-fold spidery star shape. Until now, the complexity of these
211   shapes has only been visualised via computational simulations (e.g. [1,25–29]). Using 4D in situ
212   synchrotron observations we can determine the key phenomena to inform model development, and
213   validate the microstructural simulations for real engineering alloy systems, such as Ni- and Co-
214   superalloys and alloy steels.

215   The morphological data which can be easily extracted from these unique observations is demonstrated
216   by examining zoomed regions of the Co alloy 4D images given in Fig. 4. The initial stages of growth
217   just after nucleation are captured in Fig. 4a, where two spindly primary dendrites (G1) grow very
218   rapidly into the liquid. Here, we can measure the average tip velocity per tomogram by dividing the
219   length they grow by the time per image. This provides the first value for tip velocity during the
220   solidification of a Co alloy, 11 ± 2 μm/s. (Note, this is the value just after nucleation in the temperature
221   range of 1379-1373 °C, where the growth was unobstructed, approximating unconstrained
222   conditions.)

223   New insights into the growth of secondary arms during solidification pattern formation can further be
224   analysed from the images. For example, for grain G1 in Fig. 3e,f and 4a,b, the majority of secondary
225   arm growth can be observed to be in the plane normal to the direction (depicted by a red arrow in Fig.
226   4a) in which the primaries are connected (below the field of view, FOV). This preferential growth of
227   the secondary arms is not expected crystallographically, and makes the dendritic patterns more plate-
228   like rather than a perfect 4-fold symmetric tree. This can be explained from the 3D images of G1- the
229   spacing between the first primary (brown) and second forming (blue) will be a minimum, hence the
230   secondaries that grow in this plane will have solute fields that quickly impinge, slowing their growth.
231   In the plane normal to this, the secondary tips experience free growth until their solute fields impinge
232   on the specimen walls, growing out quickly.

233   Many models for aerospace and industrial gas turbine (AGT/IGT) blades are focused on grain mis-
234   orientation and spurious grain growth[18,39]. In the Co alloy 4D images we observed, a number of
235   distinct competitive growth mechanisms were observed, which provide the first, 3D direct evidence of

7

236   the microstructural factors that promote the formation of these defects. Firstly, examining grain G1,
237   the secondary arms of the blue primary are completely restricted in three directions, two of these by
238   the walls and in one direction by the neighbouring brown primary, as shown in Fig. 4b-d. This
239   scenario does not arise in case of grains G2 and G3 due to the larger relative distance between the
240   fully developed parallel arms. Secondly, again referring to grain G1 and Fig. 4b, the primary blue
241   dendrite is clearly overgrown by a secondary growing from the brown primary dendrite. As
242   solidification progresses (Fig. 4c and d), local re-melting takes place on the lower side of the brown
243   dendrites blocking secondary arm, whilst on the top half tertiary arms form and start growing
244   upwards. This type of local remelting has been shown to lead to fragmentation in Al alloys [40–43].
245   Thirdly, in Fig. 4e-h growth competition is shown between two randomly oriented grains that nucleate
246   at almost same time and then grow in close proximity to each other. As can be seen, the growth of the
247   secondary arms in the middle of grain G2 is arrested by grain G4. These roles are reversed near the tip
248   of G4 where the secondary arms are suppressed by the growth of secondary and tertiary arms of G2,
249   although this may not seem obvious from the current viewing angle.

250   In many low temperature alloy solidification experiments, grain competition is seen to result in stray
251   grains, and re-melting is seen to culminate in pinch-off where a dendrite arm completely detaches
252   from its parent [40–43]. This kind of interaction is also reported in other metallic alloy systems where
253   experiments were performed radiographically [44], however the exact morphology, for example the
254   development of this cup-like morphology becomes apparent through a 3D tomographic examination.
255   These types of observations are critical for developing accurate models of dendrite fragmentation in
256   order to improve processing of Co and other high temperature advanced alloys, ultimately reducing
257   component costs.

3.3. Quantitative Observations

3.3.1.   Fraction solid evolution

260   These tomographic imaging observations showed that the α-Co dendrite tip velocities are remarkably
261   fast, given the slow cooling rate of 0.05 °Cs^{-1}. At this cooling rate, the difference in temperature
262   between tomograms is ~5 °C per tomogram. At the end of first and second scans, the observed solid
263   fraction was 1.6 and 8.5% respectively. The latter amounts to 25% of the overall expected solid
264   fraction just above eutectic temperature during equilibrium cooling. The rate of primary phase
265   formation (fraction solid, f_s Fig. 5a) reduces as solidification progresses and the eutectic temperature
266   is approached. The f_s as estimated from the lever and Scheil equation are also plotted in Fig. 5a, using
267   a partition coefficient, k, of 0.07 (the method adopted for estimation of k is provided in supplementary
268   note 1). The experimental solid fraction variation was close to the Scheil estimate, indicating that the
269   Hf partitions readily to the liquid upon the growth of dendrites/solid during solidification. Therefore,
270   even at this slow cooling rate the experiment is far from equilibrium.

271 ### 3.3.2. Surface area evolution

272 The evolution of surface area per unit volume of the solid (S_v) in the Co-Hf alloy is shown in Fig. 5b,

273 both for the whole volume (containing many grains) and the single largest grain (G2). Generally, S_v is

274 high during the initial stages of solidification [13,38,45] due to the high surface area to volume ratio

275 given by the high curvature nascent patterns/grains. As the solidification progresses, a steep decrease

276 in S_v is observed as a result of growth (increase in length) of each pattern, Fig. 4b and f. Eventually

277 the growth ceases, the patterns start to thicken and the local curvature reduces, Fig. 4c and g, until the

278 end of solidification, Fig. 4d and h. During thickening, the patterns also coarsen via the reduction in

279 tip curvature and coalescence of secondary arms, which reduces the surface area. After the initial

280 growth, S_v continues to reduce through combination of thickening and coarsening at a gradually

281 declining rate.

282 It is clear from the competitive growth scenarios described earlier that the impingement of patterns

283 happens at various scales and at different stages during the course of solidification. This affects the

284 overall growth and coarsening. One way to quantify this is to observe the evolution of entire solid

285 surface area normalized by the volume of liquid and solid, S_v^* as a function of fraction solid, f_s, as

286 given by Rath [46] and Cahn equation [47];

$$S_v^* = A \times f_s{}^m \times (1 - f_s)^n \qquad (1)$$

287 where, A is a proportionality constant and $m = n = 2/3$ for Cahn and $0 < (m,n) < 1$ for Rath. The

288 Rath equation is applicable for growth of features with varied aspect ratios while Cahn equation is

289 more suitable for near equiaxed (spherical) features.

290 The evolution of S_v^* as a function of f_s for the Co-Hf alloy is shown in Fig. 6, along with the Cahn and

291 the Rath curves for the current observation. The Rath curve of S_v^* for the α-Al dendritic growth in Al-

292 10 wt.% Cu, reproduced from [13] is also provided for comparison. The S_v^* in the current alloy

293 increases continuously but at a gradually reducing rate during the course of solidification.   This

294 indicates that the rate of thickening of dendrites is still faster than the rate of coalescence of secondary

295 arms. Prior studies comparing experimental coarsening rates to the Cahn and Rath equations were in

296 alloys with a very low fraction eutectic (f_e), such as the study by Limondin et al. [13] in Al 10wt% Cu

297 where their results show a f_e of <0.12, while for the Co-Hf alloy, Fig. 6, shows the f_e is approximately

298 0.6, or 60% as compared to their 12%. In the Co-Hf alloy (under continuous cooling conditions),

299 although secondary arm coalescence/coarsening is occurring it does not exceed the influence of

300 fraction solid increase upon S_v^* as the fraction primary phase is so low. As shown by Guo et al., if an

301 alloy is held isothermally (MgZn in their case), then the coarsening dominates as expected[38].

302 ## 4. Conclusions

303   A novel methodology was developed enabling 4D (3D plus time) tomographic examination of pattern

304   formation during the solidification of high temperature advanced alloys with melting temperatures

305   exceeding 1300˚C. The methodology combines three key advances: a bespoke high temperature

306   environment cell; the development of high X-ray attenuation contrast alloys; and a specimen

307   environmental encapsulation system. This method was successfully demonstrated on Ni, Fe and Co

308   alloy systems.

309   For a Co-Hf alloy system, the time-resolved tomographic datasets were examined in detail,

310   elucidating novel insights into the nucleation and growth mechanisms in Co alloys, which are a

311   critical aerospace alloy system. The results were quantitatively analysed, with quantities measured as

312   a function of time/temperature including: dendrite tip velocity, fraction solid, specific surface area and

313   coarsening. Key competitive growth and coarsening mechanisms were also elucidated. The insights

314   and quantitative data obtained will help to both inform and validate new computational models of

315   pattern formation during the liquid to solid phase transformation in high temperature advanced alloys

316   and many other systems.

317   **Acknowledgements**

325

References

[1]   W. Wang, P.D. Lee, M. McLean, A model of solidification microstructures in nickel-based superalloys: Predicting primary dendrite spacing selection, Acta Mater. 51 (2003) 2971–2987. doi:10.1016/S1359-6454(03)00110-1.

[2]   D.S. Eastwood, P.M. Bayley, H.J. Chang, O.O. Taiwo, J. Vila-Comamala, D.J.L. Brett, C. Rau, P.J. Withers, P.R. Shearing, C.P. Grey, P.D. Lee, Three-dimensional characterization of electrodeposited lithium microstructures using synchrotron X-ray phase contrast imaging, Chem. Commun. 51 (2015) 266–268. doi:10.1039/C4CC03187C.

[3]   K.A. Jackson, J.D. Hunt, Transparent compounds that freeze like metals, Acta Metall. 13 (1965) 1212–1215. doi:10.1016/0001-6160(65)90061-1.

[4]   K.A. Jackson, D.R. Uhlmann, J.D. Hunt, On the nature of crystal growth from the melt, J. Cryst. Growth. 1 (1967) 1–36. doi:10.1016/0022-0248(67)90003-6.

[5]   W.F. Kaukler, D.O. Frazier, Crystallization microstructure in transparent monotectic alloys, Nature. 323 (1986) 50–52. doi:10.1038/323050a0.

[6]   W.A. Tiller, K.A. Jackson, J.W. Rutter, B. Chalmers, The redistribution of solute atoms during the solidification of metals, Acta Metall. 1 (1953) 428–437. doi:10.1016/0001-6160(53)90126-6.

[7]   B. Li, D. Zhou, Y. Han, Assembly and phase transitions of colloidal crystals, Nat. Rev. Mater. 1 (2016) 15011. doi:10.1038/natrevmats.2015.11.

[8]   E.W.J. Miller, J. Beech, In-situ radiographic observations of alloy solidification, Metallography. 5 (1972) 298–300. doi:10.1016/0026-0800(72)90009-2.

[9]   J. Wang, P.D. Lee, R.W. Hamilton, M. Li, J. Allison, The kinetics of Fe-rich intermetallic formation in aluminium alloys: In situ observation, Scr. Mater. 60 (2009) 516–519. doi:10.1016/j.scriptamat.2008.11.048.

[10]   P.D. Lee, J.D. Hunt, Hydrogen porosity in directional solidified aluminium-copper alloys:in situ observation, Acta Mater. 45 (1997) 4155–4169. doi:10.1016/S1359-6454(97)00081-5.

[11]   H. Yasuda, T. Nagira, M. Yoshiya, N. Nakatsuka, A. Sugiyama, K. Uesugi, K. Umetani, Development of X-ray Imaging for Observing Solidification of Carbon Steels, ISIJ Int. 51 (2011) 402–408. doi:10.2355/isijinternational.51.402.

[12]   N. Limodin, L. Salvo, M. Suéry, M. DiMichiel, In situ investigation by X-ray tomography of the overall and local microstructural changes occurring during partial remelting of an Al-15.8 wt.% Cu alloy, Acta Mater. 55 (2007) 3177–3191. doi:10.1016/j.actamat.2007.01.027.

[13]   N. Limodin, L. Salvo, E. Boller, M. Suéry, M. Felberbaum, S. Gaillègue, K. Madi, In situ and real-time 3-D microtomography investigation of dendritic solidification in an Al-10 wt.% Cu alloy, Acta Mater. 57 (2009) 2300–2310. doi:10.1016/j.actamat.2009.01.035.

[14]   M. Suéry, S. Terzi, B. Mireux, L. Salvo, J. Adrien, E. Maire, Fast in situ x-ray microtomography observations of solidification and semisolid deformation of Al-Cu alloys, JOM. 64 (2012) 83–88. doi:10.1007/s11837-011-0219-7.

[15]   K.M. Kareh, P.D. Lee, R.C. Atwood, T. Connolley, C.M. Gourlay, Revealing the micromechanisms behind semi-solid metal deformation with time-resolved X-ray tomography, Nat Commun. 5 (2014) 4464. doi:10.1038/ncomms5464.

[16]   S. Karagadde, P.D. Lee, B. Cai, J.L. Fife, M.A. Azeem, K.M. Kareh, C. Puncreobutr, D. Tsivoulas, T. Connolley, R.C. Atwood, Transgranular liquation cracking of grains in the semi-solid state., Nat. Commun. 6 (2015) 8300. doi:10.1038/ncomms9300.

[17]   S. Karagadde, L. Yuan, N. Shevchenko, S. Eckert, P.D. Lee, 3-D microstructural model of freckle formation validated using in situ experiments, Acta Mater. 79 (2014) 168–180.

11

372   doi:10.1016/j.actamat.2014.07.002.

373   [18]   J.D. Miller, L. Yuan, P.D. Lee, T.M. Pollock, Simulation of diffusion-limited lateral growth of
374   dendrites during solidification via liquid metal cooling, Acta Mater. 69 (2014) 47–59.
375   doi:10.1016/j.actamat.2014.01.035.

376   [19]   A.J. Clarke, D. Tourret, S.D. Imhoff, P.J. Gibbs, K. Fezzaa, J.C. Cooley, W.K. Lee, A. Deriy,
377   B.M. Patterson, P.A. Papin, K.D. Clarke, R.D. Field, J.L. Smith, X-ray imaging and controlled
378   solidification of Al-Cu alloys toward microstructures by design, Adv. Eng. Mater. 17 (2015)
379   454–459. doi:10.1002/adem.201400469.

380   [20]   J.A. Dantzig, M. Rappaz, Solidification, EPFL press, 2009.

381   [21]   H.A. Bale, A. Haboub, A.A. MacDowell, J.R. Nasiatka, D.Y. Parkinson, B.N. Cox, D.B.
382   Marshall, R.O. Ritchie, Real-time quantitative imaging of failure events in materials under
383   load at temperatures above 1,600 °C, Nat. Mater. 12 (2012) 40–46. doi:10.1038/nmat3497.

384   [22]   L. Yuan, P.D. Lee, A new mechanism for freckle initiation based on microstructural level
385   simulation, Acta Mater. 60 (2012) 4917–4926. doi:10.1016/j.actamat.2012.04.043.

386   [23]   N. D'Souza, M.G. Ardakani, M. McLean, B. A. Shollock, Directional and single-crystal
387   solidification of Ni-base superalloys: Part I - The role of curved isotherms on grain selection,
388   Metall. Mater. Trans. A. 31 (2000) 2877–2886. doi:10.1007/BF02830351.

389   [24]   M.G. Ardakani, N. D'Souza, B.A. Shollock, M. McLean, Directional and single-crystal
390   solidification of Ni-base superalloys: Part II. Coincidence site lattice character of grain
391   boundaries, Metall. Mater. Trans. A. 31 (2000) 2887–2893. doi:10.1007/BF02830350.

392   [25]   D. Tourret, A. Karma, Three-dimensional dendritic needle network model for alloy
393   solidification, Acta Mater. 120 (2016) 240–254. doi:10.1016/j.actamat.2016.08.041.

394   [26]   L. Yuan, P.D. Lee, Dendritic solidification under natural and forced convection in binary
395   alloys: 2D versus 3D simulation, Model. Simul. Mater. Sci. Eng. 18 (2010) 55008.
396   doi:10.1088/0965-0393/18/5/055008.

397   [27]   D. Li, X.-Q. Chen, P. Fu, X. Ma, H. Liu, Y. Chen, Y. Cao, Y. Luan, Y. Li, Inclusion flotation-
398   driven channel segregation in solidifying steels, Nat. Commun. 5 (2014) 5572.
399   doi:10.1038/ncomms6572.

400   [28]   T. Haxhimali, A. Karma, F. Gonzales, M. Rappaz, Orientation selection in dendritic
401   evolution., Nat. Mater. 5 (2006) 660–664. doi:10.1038/nmat1693.

402   [29]   N. Bergeon, D. Tourret, L. Chen, J. Debierre, R. Gu, A. Ramirez, B. Billia, A. Karma, R.
403   Trivedi, Spatiotemporal dynamics of oscillatory cellular patterns in three-dimensional
404   directional solidification Supplementary information, 226102 (2013) 1–7.
405   doi:10.1103/PhysRevLett.110.226102.

406   [30]   K. Ishida, T. Nishizawa, The Co-Hf (Cobalt-Hafnium) system, J. Phase Equilibria. 12 (1991)
407   424–427. doi:10.1007/BF02645960.

408   [31]   H. Baker, ASM Handbook: Alloy Phase Diagram, Met. Park. OH, USA ASM Int. 3 (1992).

409   [32]   W.H. McMaster, N. Kerr Del Grande, J.H. Mallett, J.H. Hubbell, Compilation of x-ray cross
410   sections UCRL-50174, sections I, II revision 1, III, IV, At. Data Nucl. Data Tables. 8 (1970)
411   443–444. doi:10.1016/S0092-640X(70)80026-2.

412   [33]   C. Puncreobutr, P.D. Lee, K.M. Kareh, T. Connolley, J.L. Fife, A.B. Phillion, Influence of Fe-
413   rich intermetallics on solidification defects in Al-Si-Cu alloys, Acta Mater. 68 (2014) 42–51.
414   doi:10.1016/j.actamat.2014.01.007.

415   [34]   A.K. Vasudévan, J.J. Petrovic, A comparative overview of molybdenum disilicide composites,
416   Mater. Sci. Eng. A. 155 (1992) 1–17. doi:10.1016/0921-5093(92)90308-N.

417   [35]   http://Kanthal.Com/En/Products/Furnace-Products-and-Heating-Systems/Electric-Heating-

418   Elements/Molybdenum-Disilicide-Heating-Elements/, (n.d.).

419   [36]   S. Titarenko, V. Titarenko, A. Kyrieleis, P.J. Withers, A ring artifact suppression algorithm
420   based on a priori information, Appl. Phys. Lett. 95 (2009) 7–10. doi:10.1063/1.3211956.

421   [37]   P. Kurowski, Thermal Analysis with SolidWorks Simulation 2014, SDC Publications, 2014.

422   [38]   E. Guo, A.B. Phillion, B. Cai, S. Shuai, D. Kazantsev, T. Jing, P.D. Lee, Dendritic evolution
423   during coarsening of Mg-Zn alloys via 4D synchrotron tomography, Acta Mater. 123 (2017)
424   373–382. doi:10.1016/j.actamat.2016.10.022.

425   [39]   X. Yang, D. Ness, P.D. Lee, N. D'Souza, Simulation of stray grain formation during single
426   crystal seed melt-back and initial withdrawal in the Ni-base superalloy CMSX4, Mater. Sci.
427   Eng. A. 413–414 (2005) 571–577. doi:10.1016/j.msea.2005.09.058.

428   [40]   D. Ruvalcaba, R.H. Mathiesen, D.G. Eskin, L. Arnberg, L. Katgerman, In situ observations of
429   dendritic fragmentation due to local solute-enrichment during directional solidification of an
430   aluminum alloy, Acta Mater. 55 (2007) 4287–4292. doi:10.1016/j.actamat.2007.03.030.

431   [41]   L. Arnberg, R.H. Mathiesen, The real-time, high-resolution X-ray video microscopy of
432   solidification in aluminum alloys, JOM. 59 (2007) 20–26. doi:10.1007/s11837-007-0099-z.

433   [42]   S. Ji, The fragmentation of primary dendrites during shearing in semisolid processing, J.
434   Mater. Sci. 38 (2003) 1559–1564. doi:10.1023/A:1022945219926.

435   [43]   B. Cai, J. Wang, A. Kao, K. Pericleous, A.B. Phillion, R.C. Atwood, P.D. Lee, 4D synchrotron
436   X-ray tomographic quantification of the transition from cellular to dendrite growth during
437   directional solidification, Acta Mater. 117 (2016) 160–169.
438   doi:10.1016/j.actamat.2016.07.002.

439   [44]   S. Boden, S. Eckert, B. Willers, G. Gerbeth, X-ray radioscopic visualization of the solutal
440   convection during solidification of a Ga-30 Wt Pct in alloy, Metall. Mater. Trans. A Phys.
441   Metall. Mater. Sci. 39 A (2008) 613–623. doi:10.1007/s11661-007-9462-5.

442   [45]   J.W. Gibbs, K.A. Mohan, E.B. Gulsoy, A.J. Shahani, X. Xiao, C.A. Bouman, M. De Graef,
443   P.W. Voorhees, The Three-Dimensional Morphology of Growing Dendrites, Sci. Rep. 5
444   (2015) 11824. doi:10.1038/srep11824.

445   [46]   B.B. Rath, C.S. Pande, An analytical description of overall phase transformation kinetics
446   applied to the recrystallization of pure iron, Acta Mater. 59 (2011) 7538–7545.
447   doi:10.1016/j.actamat.2011.09.027.

448   [47]   J.W. Cahn, Significance of average mean curvature and its determination by quantitative
449   metallography, Trans. Metall. Soc. AIME. 239 (1967) 610. doi:10.4319/lo.2013.58.2.0489.
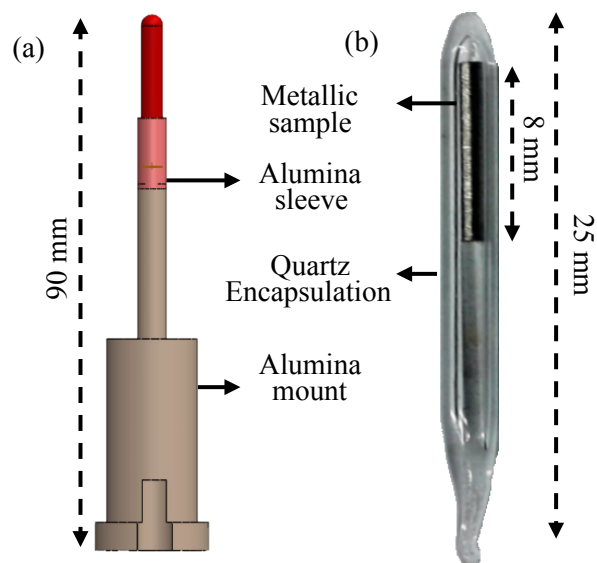
450

451

452

List of Figures

Fig. 1. (a) Schematic of the sample module with alumina sample mount and quartz encapsulated sample and (b) image of the as-encapsulated sample, held in place at one end of the encapsulation by a quartz rod.
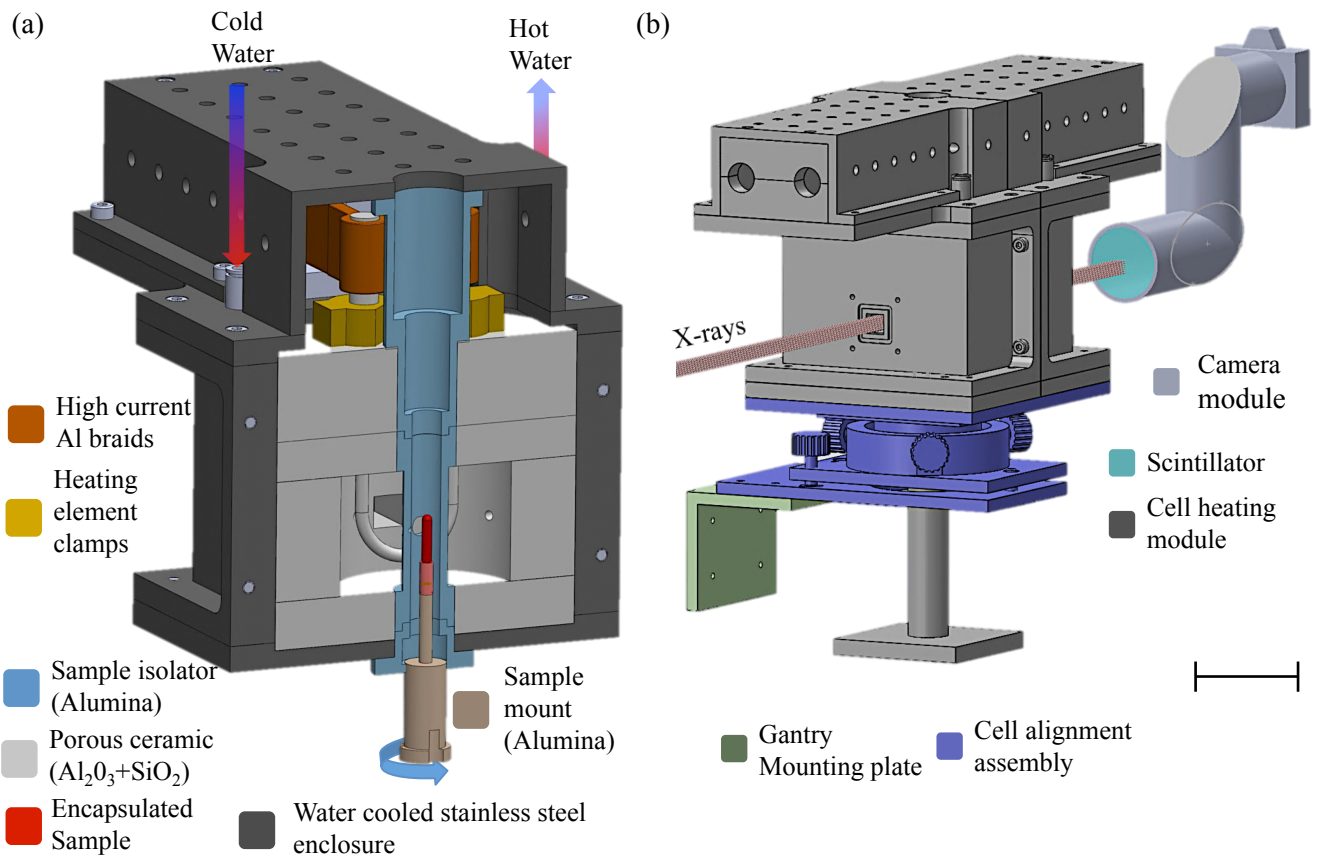
Fig. 2. (a) Schematic of one half of environmental cell with heating and sample module and (b) schematic of the environmental cell setup at the I12 beamline of Diamond Light Source. Scale bar = 32.5 mm.
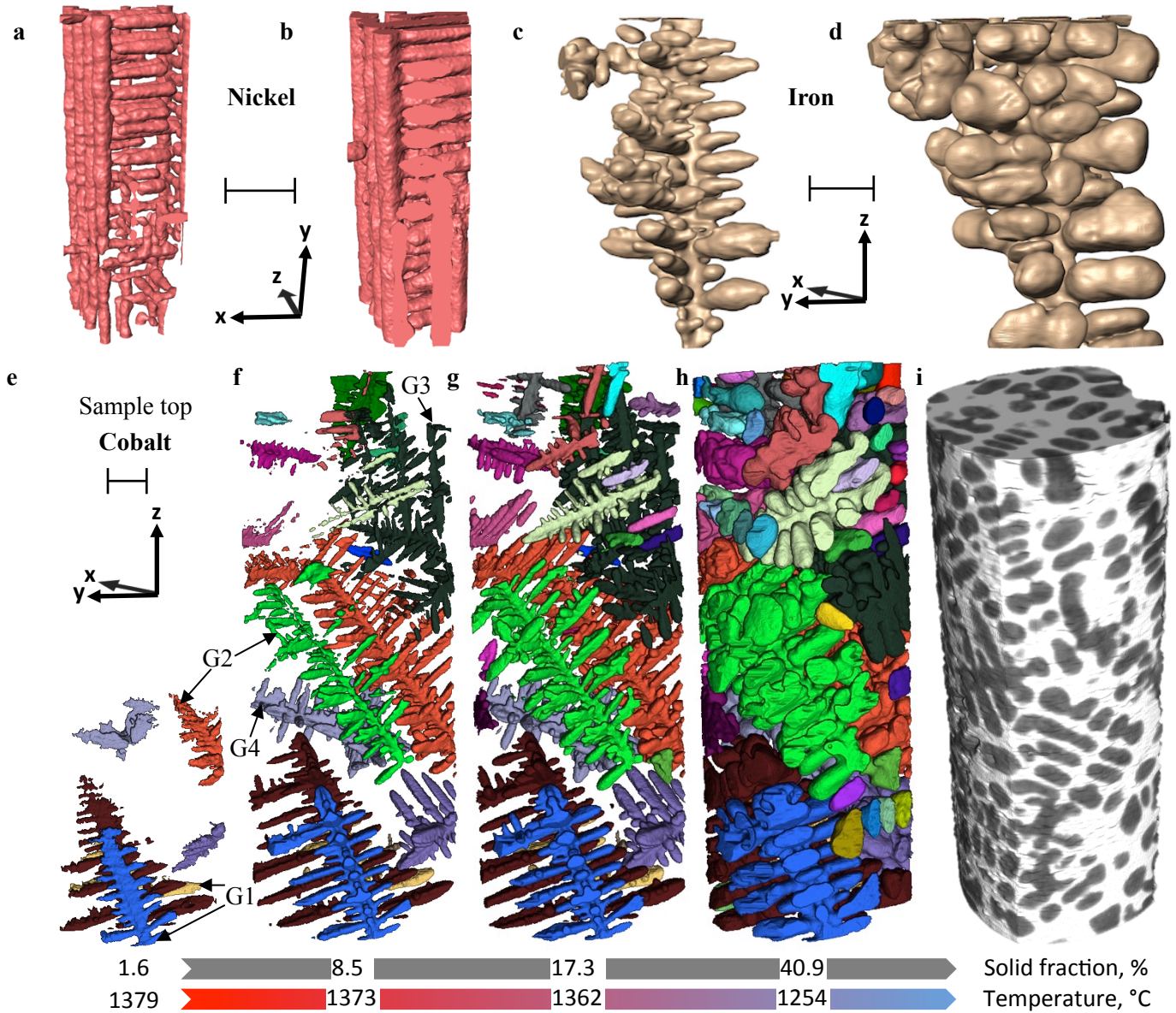
Fig. 3. The 3D evolution of dendritic patterns in Ni-14 wt. % Hf, Fe-11 wt. % Hf and Co-18 wt. % Hf alloys during solidification at a cooling rate of 0.05 °Cs⁻¹ are shown. The interlocking FCC α-Ni dendritic patterns at 495 and 1496 s after the start of solidification are shown in (a) and (b) respectively. The development of a single δ-Fe pattern during solidification via thickening, coarsening and coalescence mechanisms captured 396 and 3960 s are shown in (c) and (d) respectively. The development of α-Co patterns during solidification of the Co alloy is shown in (e)-(h). The corresponding temperatures and volume fractions are provided below each subfigure, where, (e) is captured at ~3 °C below the equilibrium liquidus temperature of the alloy and (h) at ~24 °C above the reported equilibrium eutectic temperature. The raw data of the reconstructed volume corresponding to (h) is shown in (i). Scale bar = 200 μm.
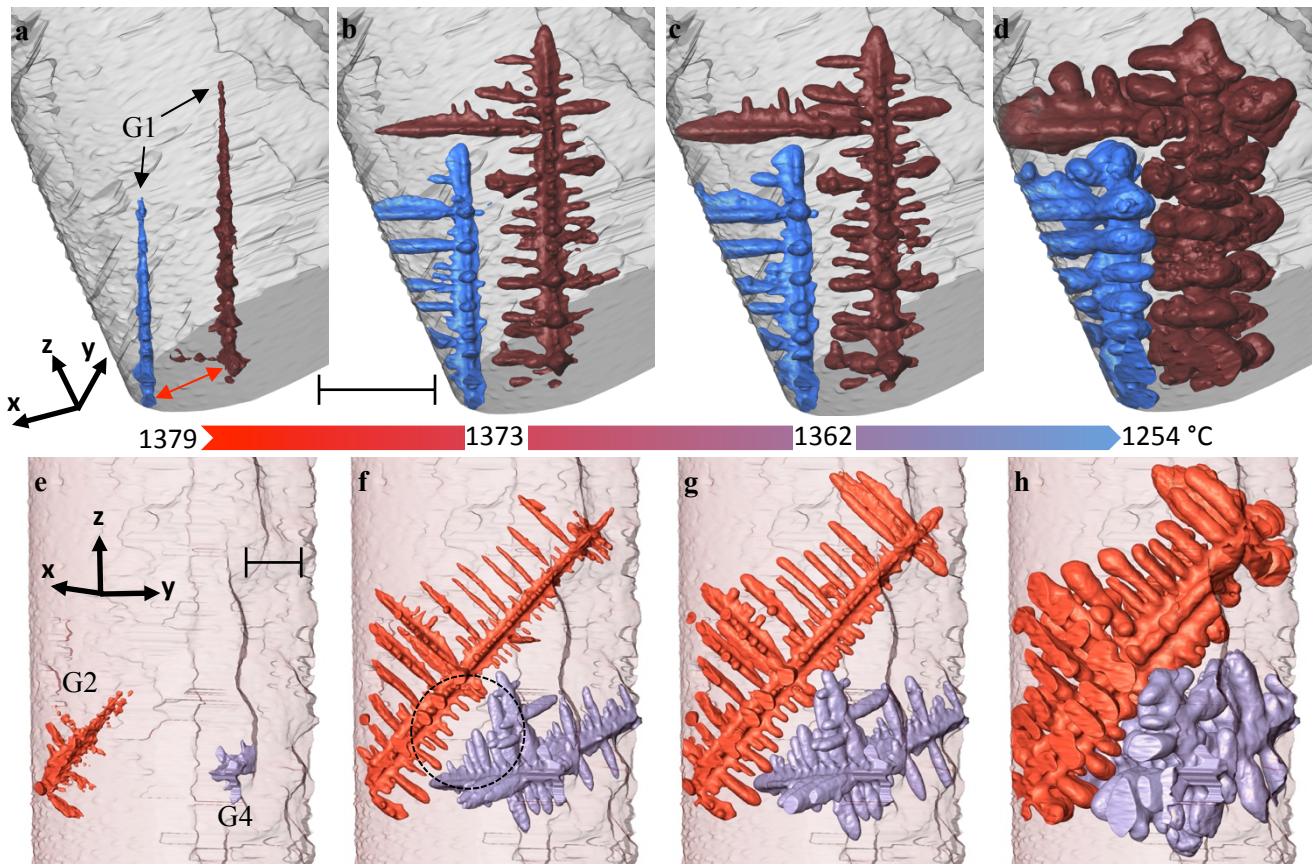
Fig. 4. Competitive growth, a case of interaction between dendritic arms of the same grain (G1) is shown in (a-d). The corresponding temperatures are shown below each sub figure. The blue dendritic arm is intercepted by a tertiary arm from the large brown dendrite. A case of competition between two different dendritic grains (G2 and G4) captured at same temperatures in a sample space above G1 is shown in (e-h). Here, the growth of secondary arms of the (larger) orange grain in the middle of the dendrite are restricted by the secondary arms of grey grains. Similarly, the secondary arms at the front end of G4 is restricted by G2. Scale bar = 200 μm.
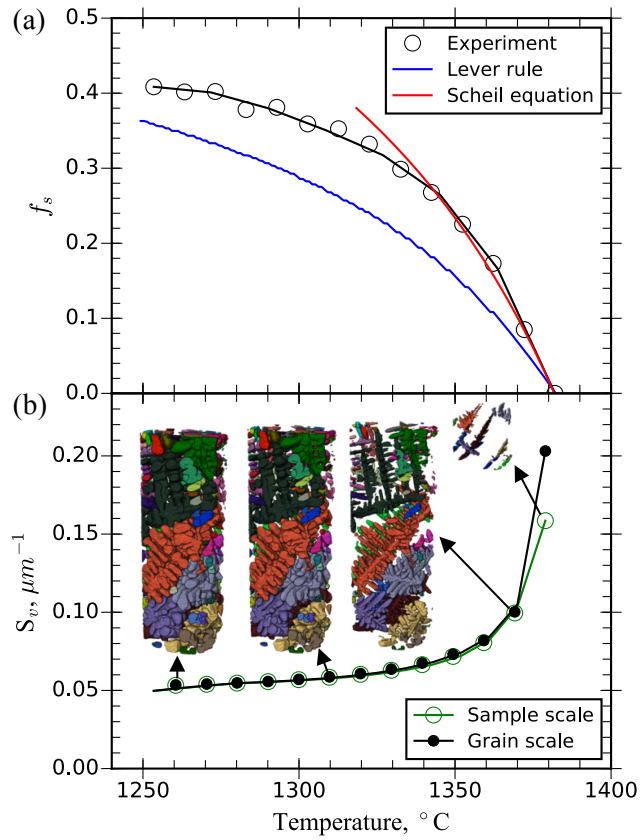
Fig. 5. The evolution of (a) volume fraction of α-Co phase during solidification of Co-18wt. % Hf alloy at a cooling rate of 0.05 °Cs⁻¹. Lever rule and Scheil estimates are also provided and (b) evolution of volume normalised surface area, S_v, of α-Co dendritic patterns with temperature, on a single grain and sample scale.
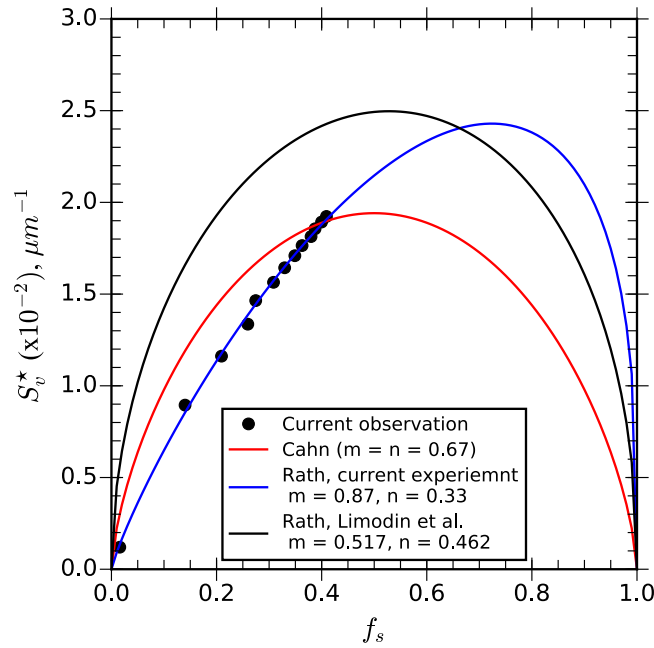
Fig. 6. The evolution of total volume normalized surface area of the solid during solicitation in the current Co-18wt. % Hf alloy is shown. The behaviour is interpreted in terms of Rath and Cahn equations. The observed/Rath plot of the α-Al dendritic structure during solidification in A1-10Cu as reported by Limodin et at.[13] (black graph) is also provided along side for comparison.
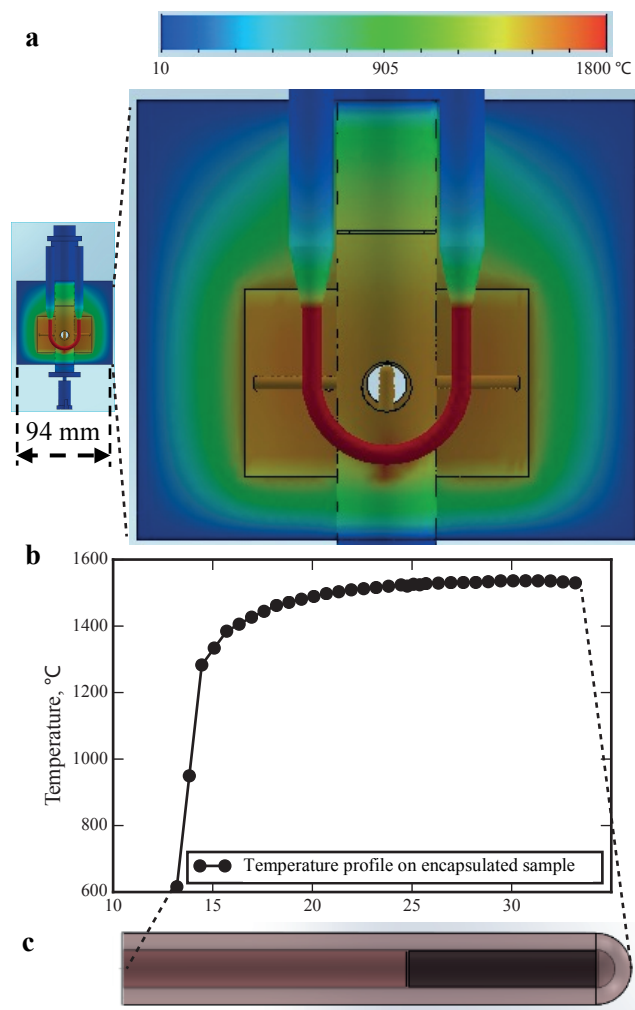
Supplementary

Supplementary Movie M1 | Evolution of α-Co dendritic patterns: Sequence of 3D X-ray tomographic images showing the evolution of α-Co dendritic patterns in high contrast Co-18 wt. % Hf alloy during solidification at a cooling rate of 0.05 °Cs^{-1}. The outer oxide ring is removed by image processing for the sake of visualization.

Supplementary Movie M2 | 2D images of as-acquired tomograms: As acquired 2D time series showing the evolving morphology of α-Co dendritic patterns in high contrast Co-18 wt. % Hf alloy during solidification at a cooling rate of 0.05 °Cs^{-1}. The white arrows indicate the location where an instance of competitive growth is occurring between two intersecting dendrites.

Supplementary Note 1 | Estimation of partitioning coefficient: During solidification of an alloy, the separation of solute between solid and liquid phases is interpreted in terms of partitioning coefficient or the Scheil proportionality constant, k. A schematic of the hypoeutectic binary alloy system is shown in Fig. S1a, k is estimated by the ratio of the concentration of the solid (C_S) to the concentration of liquid C_L. Under equilibrium cooling conditions, the Co-Hf alloy system has a liquidus line with increasing slope as the eutectic composition is approached, as shown in Fig. S1b, after Ishida, K. and Nishizawa[40]. The Scheil proportionality constant k measured from the equilibrium phase diagram was found to be 0.11, however a k of 0.07 is used in the calculation so as to make the Scheil graph concurrent with the 0% solid fraction on the composition axis (Fig. 3a).
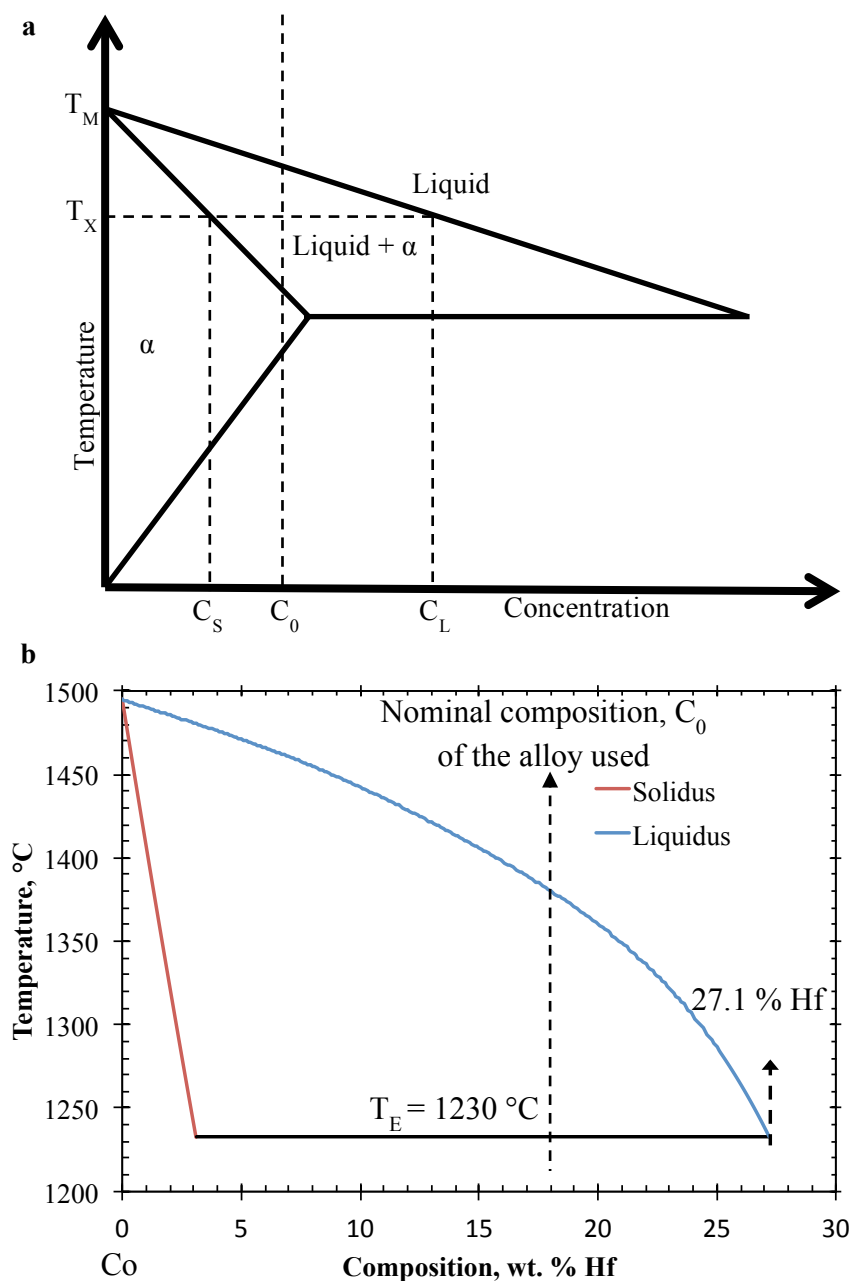
Supplementary Fig. S1. (a) Schematic of the hypoeutectic region of a binary phase diagram, where C_L and C_S represent the concentration of liquid and solid respectively, C_0 is the nominal composition of alloy of interest, T_M the melting point of the pure species and T_X is a temperature of interest. (b) hypoeutectic region of the the Co-Hf phase diagram, after Ishida and Nishizawa [30].

Supplementary Fig. S2. Thermal modeling of (a) temperature distribution inside the furnace shown here in the front view, (b) temperature profile on the sample encapsulation (schematically shown in (c)).